Topography of the Polar Layered Deposits of Mars

DANIEL DZURISIN AND KARL R. BLASIUS

Division of Geological and Planetary Sciences, California Institute of Technology, Pasadena, California 91125

Synthesis of polar topographic data derived from the Mariner 9 radio occultation, ultraviolet spectrometer, and television imaging experiments provides new information on the behavior of polar volatiles and the topographic configuration of the martian polar layered deposits. Gentle slopes in the vicinity of the south pole may serve to shift the point of minimum annual solar insolation from the pole to a site within the perimeter of the offset residual frost cap. Localized defrosting which gives rise to the dark-banded appearance of both residual caps correlates with a series of outward-facing slopes descending from central topographic highs. Stability of the volatile involved apparently is largely insolation controlled. The south polar residual cap lies entirely higher (at lower pressure) than the northern cap, implying that the south residual cap is an unlikely site for any permanent surface deposit of solid carbon dioxide. Photogrammetric models of both residual caps reveal a series of regularly spaced topographic undulations descending from central topographic highs within the underlying layered deposits. Scarplike to troughlike in cross section, these features slope 1°–5° and are 100–1000 m in local relief. The south polar layered deposits lie almost entirely at higher elevations than those in the north. Total thickness of the deposits is inferred to be 1–2 km in the south and 4–6 km in the north.

INTRODUCTION

Mariner 9 has provided a wealth of new information for the polar regions of Mars. This paper deals specifically with polar topographic data, especially as they apply to the behavior of polar volatiles and to the topographic configuration of polar layered deposits. The effect of local heights and slopes on volatile stability in the polar regions is examined and discussed. Preliminary conclusions on the nature of polar volatiles based on theoretical considerations and incomplete topographic data [*Cutts*, 1973*b*; *Murray and Malin*, 1973*b*] are reexamined on the basis of more detailed topographic information.

Murray and Malin [1973*a*] and *Cutts* [1973*a*] have suggested that clues to the genesis of the polar layered deposits may be obtained from their present topographic configuration. We examine those authors' differing interpretations of the dark bands which transect both residual frost caps in light of a new semiquantitative topographic description of the underlying layered deposits.

DATA DESCRIPTION

Mariner 9 provided four potential sources of topographic information for the martian polar regions: (1) *S* band radio occultation, (2) infrared interferometer spectrometer, (3) ultraviolet spectrometer (UVS), and (4) television imaging. Unfavorable viewing geometry of the martian polar regions precludes the acquisition of reliable ground-based radar or CO_2 pressure data.

The *S* band radio occultation experiment provided 12 useful occultation points within the boundary of the south polar layered deposits and 3 within the northern deposits [*Kliore et al.*, 1973]. Detailed analysis of polar topography is not possible from these data alone, owing to low spatial density of the occultation measurements. Although the infrared interferometer spectrometer has provided some data on equatorial and mid-latitude topography [*Conrath et al.*, 1973], no polar topographic information is currently available.

Preliminary analysis of several hundred spectra from the Mariner 9 ultraviolet spectrometer has been completed by K. Pang of the Jet Propulsion Laboratory and C. W. Hord of the University of Colorado. Analysis is continuing in an attempt to eliminate small perturbing effects apparently associated with local atmospheric inhomogeneities.

Finally, Mariner 9 returned more than 1100 television frames of areas poleward of 65° latitude, over half of high (B camera) resolution. Some of the B camera stereo images of the south polar residual frost cap were previously processed to produce high-resolution point elevation maps [*Blasius*, 1973]. Six more B frame photogrammetric models are presented and are combined with wide-angle A frame models to produce generalized topographic maps of the north and south polar residual frost caps and underlying layered deposits.

SOUTH POLAR REGION

Large-Scale Topography

Both the radio occultation and the ultraviolet spectrometer data in the south polar region suggest that the area is topographically complex [*Kliore et al.*, 1973; K. Pang and C. W. Hord, personal communication, 1974] (see Figure 1, Table 1). Note especially the existence of an arcuate scarp approximately 1300 km long centered near 83°S, 266°W (see upper right of Figure 1). *Wilhelms* [1973] has interpreted the feature as the rim of a major impact basin roughly 850 km in diameter, and *Pang* [1972] has suggested that the basin may be responsible for the offset of the south polar residual frost cap. For a perfect sphere the point of minimum annual solar insolation lies at the point(s) on the surface whose local normal is parallel to the spin axis. Should the topographic expression of an ancient impact basin be preserved in the vicinity of the pole, its slopes would serve to shift the point of minimum annual solar insolation away from the rotational pole to some lower latitude. The offset of the south polar residual cap is consistent with a small local slope at the pole toward the center of the basin.

K. Pang and C. W. Hord (personal communication, 1974) report that preliminary analysis of the south polar UVS data suggests a broad quasi-circular depression approximately 3 km deep which correlates with the location of the presumed im-

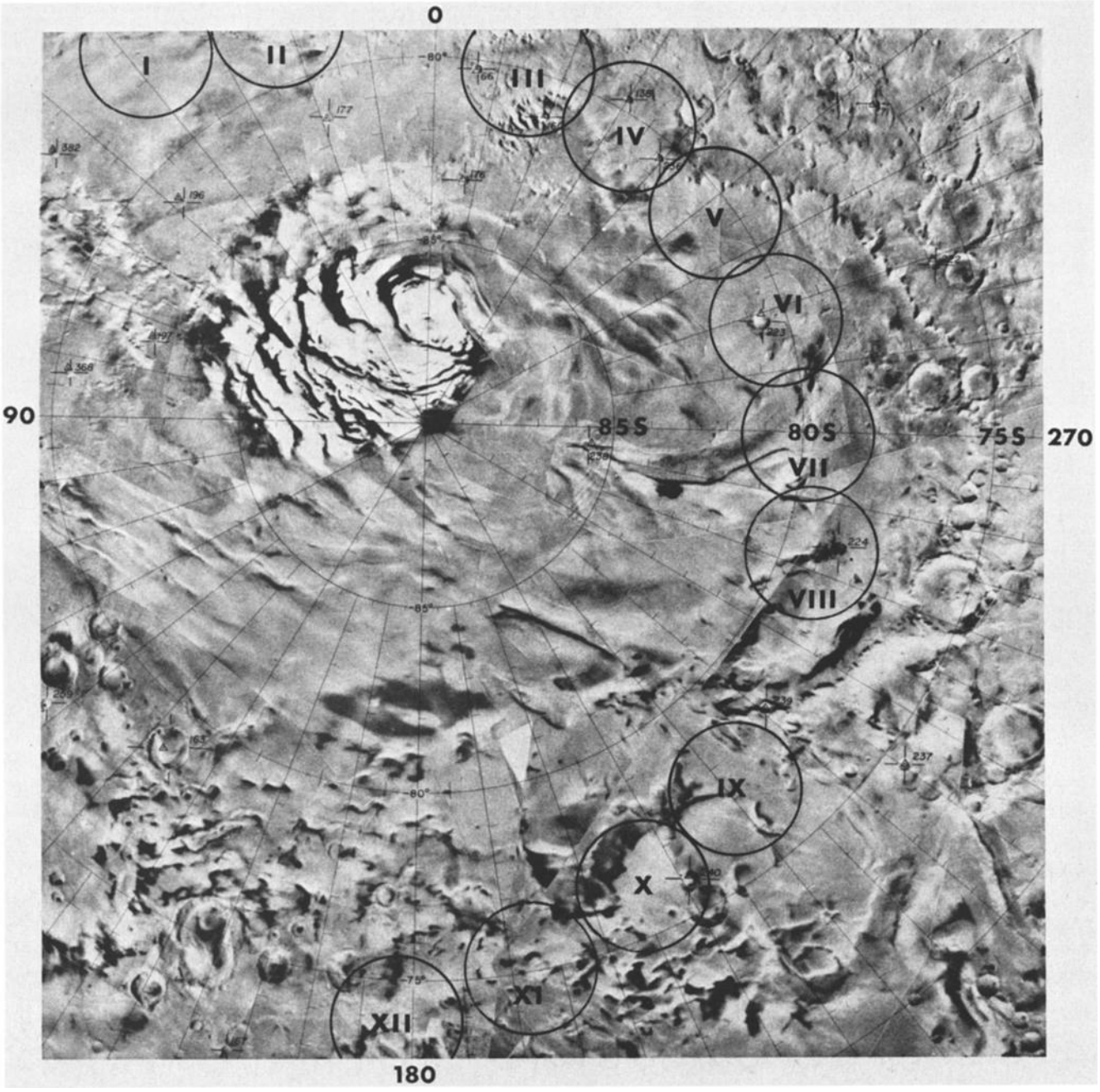

Fig. 1. Enlarged segment of the United States Geological Survey semicontrolled photomosaic of the region poleward of 65°S showing the planimetric configuration of the residual polar frost cap and the polar layered deposits. Circles enclose locations of radio occultation-derived radii measurements (see Table 1). Small triangles on the map denote points in the Mariner 9 control net used to establish the system of martian coordinates. Original scale of the USGS photomosaic was 1 : 5,000,000.

pact basin. A local slope of about 0.5° inward toward the basin's center is indicated at the pole. Modeling errors apparently associated with local atmospheric inhomogeneities have been recognized, however, and may contribute to the apparent relief of the basin. Radio occultation data near the basin (Figure 1, Table 1) suggest a broad depression about 1 km deep but do not sample the basin's center. Although details of the basin's topography remain unresolved at this time, we adopt the UVS result of about 3 km maximum depth in subsequent discussions.

In addition to the large-scale UVS and occultation-derived data, a photogrammetric model of the residual south polar frost cap has been prepared from wide-angle A camera photography (model A of Table 2; Table 3). For this and other models to be presented, relative elevations of a network of small features visible in both frames of Mariner 9 stereo pairs have been calculated from basic photogrammetric principles according to a recently developed analytic scheme for stereo analysis of spacecraft images [*Blasius*, 1973]. Topographic contours have then been interpolated between points to produce conventional topographic maps. Since no ground control points of known elevation are available in the polar regions, imprecisely known orbital and viewing parameters must be used to establish a reference datum for each model. An estimate of the tilt uncertainty obtained by comparing several overlapping models (not all in the polar regions) in-

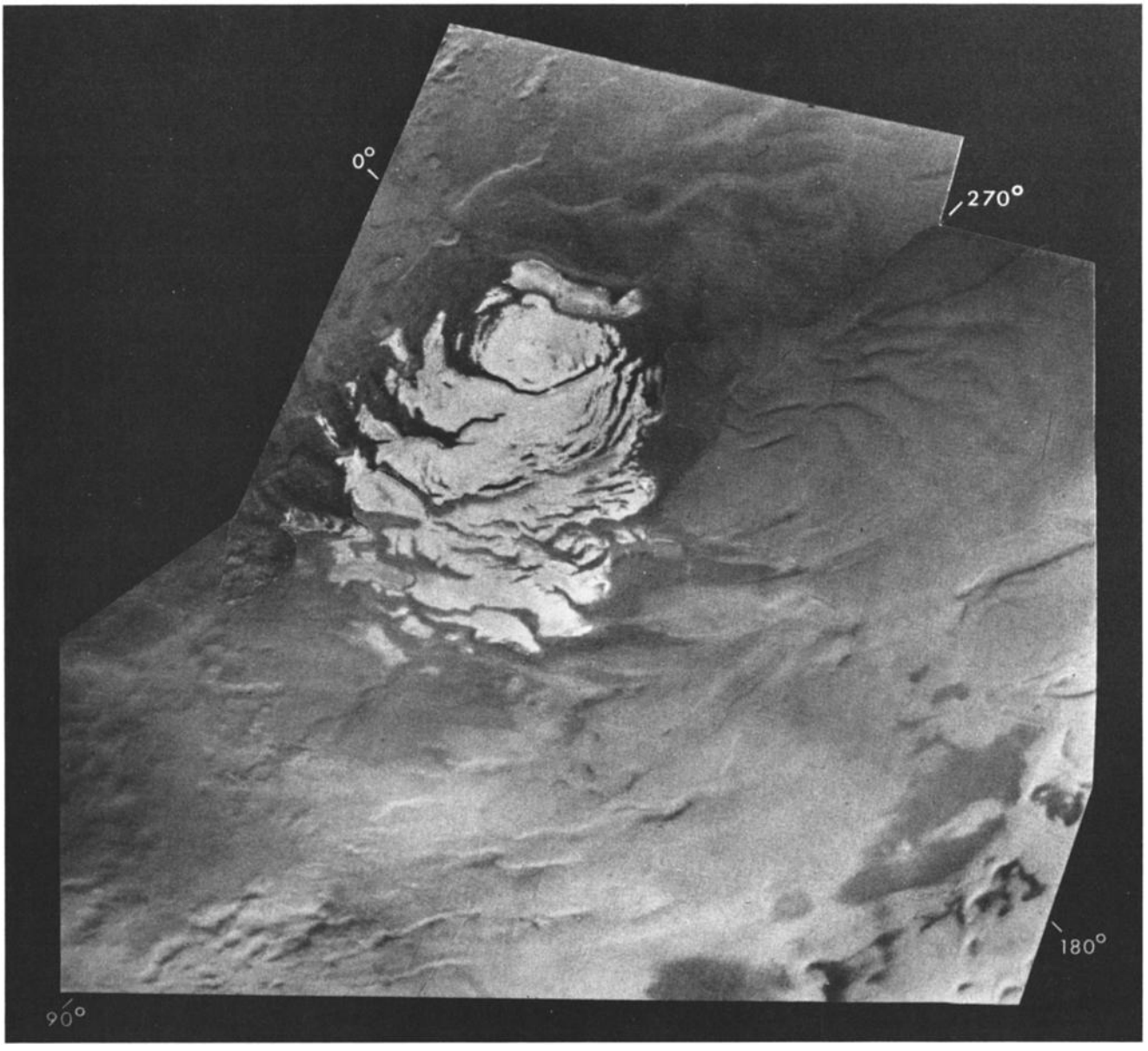

Fig. 2. Photomosaic of the south polar residual frost cap at A frame resolution. It is argued in the text that the dark bands arise from selective defrosting of a series of outward-facing slopes descending from a central topographic high near 87°S, 0°W. Two photographs used in the mosaic have been computer enhanced at the Image Processing Lab of NASA's Jet Propulsion Laboratory.

TABLE 1. Polar Occultation Points [From *Kliore et al.*, 1973]

Point	Radius, km
South Polar Region (Figure 1)	
I-408X (noisy)	3381.5
II-410X (noisy)	3380.9
III-414X (noisy)	3383.9
IV-416X	3379.4
V-418X (noisy)	3379.8
VI-420X	3379.9
VII-422X (noisy)	3380.1
VIII-424X (noisy)	3380.0
IX-428X (noisy)	3381.4
X-430X (noisy)	3381.9
XI-432X (noisy)	3380.6
XII-434X	3383.8
North Polar Region (Figure 15)	
XIII-374N (noisy)	3376.6
XIV-376N	3376.8
XV-378N	3378.1

dicates that regional tilts can disagree by as much as 2.5°. Figures 2 and 3 combine the south polar A frame information with high-resolution B frame models to be discussed in a later section. An attempt has been made to blend the two sources of information into a generalized topographic map by adjusting the tilts of the B frame models within uncertainty limits to achieve internal consistency.

Figure 3 reveals what appears to be a broad, domical form centered near 87°S, 0°W. Since the residual frost is interrupted by numerous defrosted bands, we assume that the frost is relatively thin (<100 m) and conforms to topography of the underlying layered deposits. Details of high-resolution models outlined in Figure 3 suggest that the deposits exhibit a series of topographic undulations descending from the central high near 87°S, 0°W. Slopes associated with these features are generally outward-facing from the central high. They are not exclusively equatorward-facing, since the topographic high is slightly offset from the rotational pole.

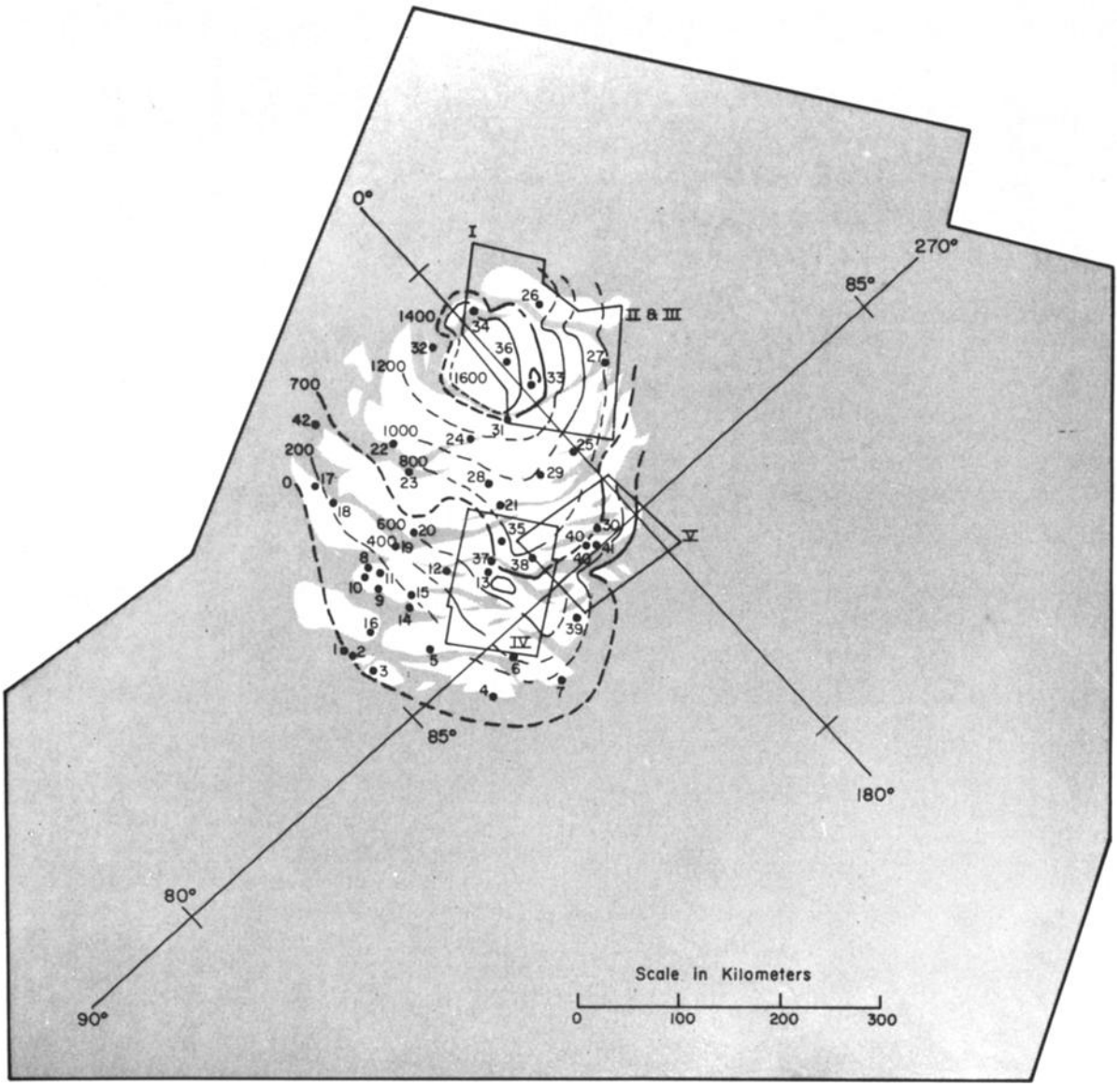

Fig. 3. Generalized topographic map of the south polar residual frost cap. The map was constructed by combining information from a single A frame photogrammetric model (model A) with that from five high-resolution B frame models. Locations of the B frame models have been outlined to illustrate the areas for which high-resolution information is available. Point elevations for the A frame model are listed in Table 3. Planetary curvature has been removed from the models by assuming a spherical planet with a radius of 3382 km. Note irregular contour interval; contours labeled in meters.

TABLE 2. Stereo Models

Model	Photo DAS	Approximate Location	Ground Resolution (Per 2 Picture Elements), m	Estimated Elevation Uncertainty, m	Observed Elevation Uncertainty, m
I	6029873	85.7°S	227	80	65
	3717850	354.5°W	247		
II	3466690	87.3°S	260	75	65
	3574350	344.5°W	267		
III	7791983	87.3°S	233	85	85
	3574350	344.5°W	267		
IV	3466620	86.7°S	293	80	75
	7900063	83.6°W	207		
V	6784823	89.0°S	227	85	80
	9698649	90.0°W	213		
VI	13352795	79.6°N	660	250	250
	13463258	343.3°W	473		
A	8295814	90°S	1940	750	800
	8331864		1900		
B	13317545	90°N	5920	2500	2500
	13353320		5727		

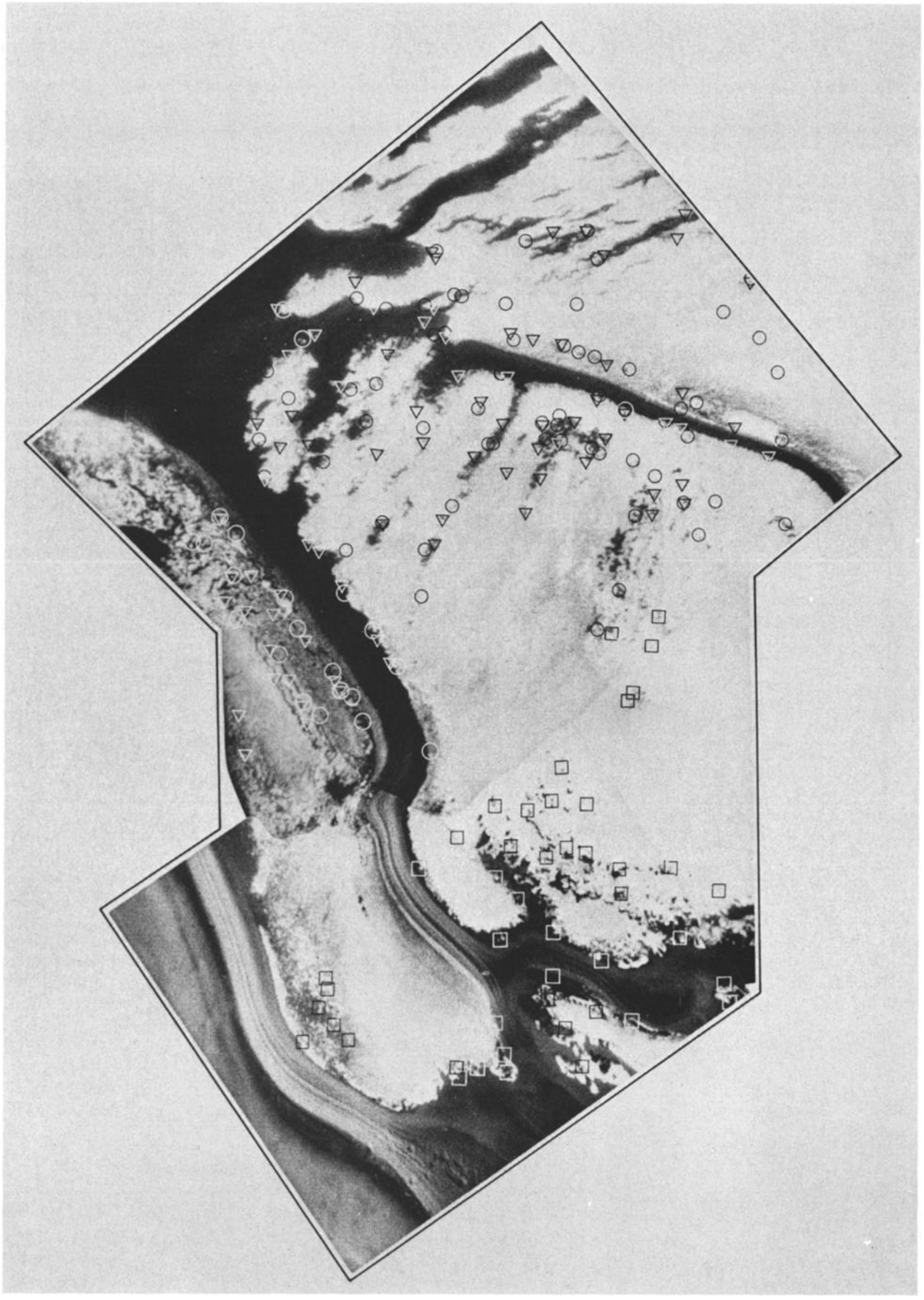

Fig. 4. Photomosaic of an area centered at 86.5°S, 0°W for which three high-resolution photogrammetric models have been constructed (Figures 5, 7, 8). Squares, triangles, and circles enclose point features for which relative elevations have been calculated in models I, II, and III, respectively.

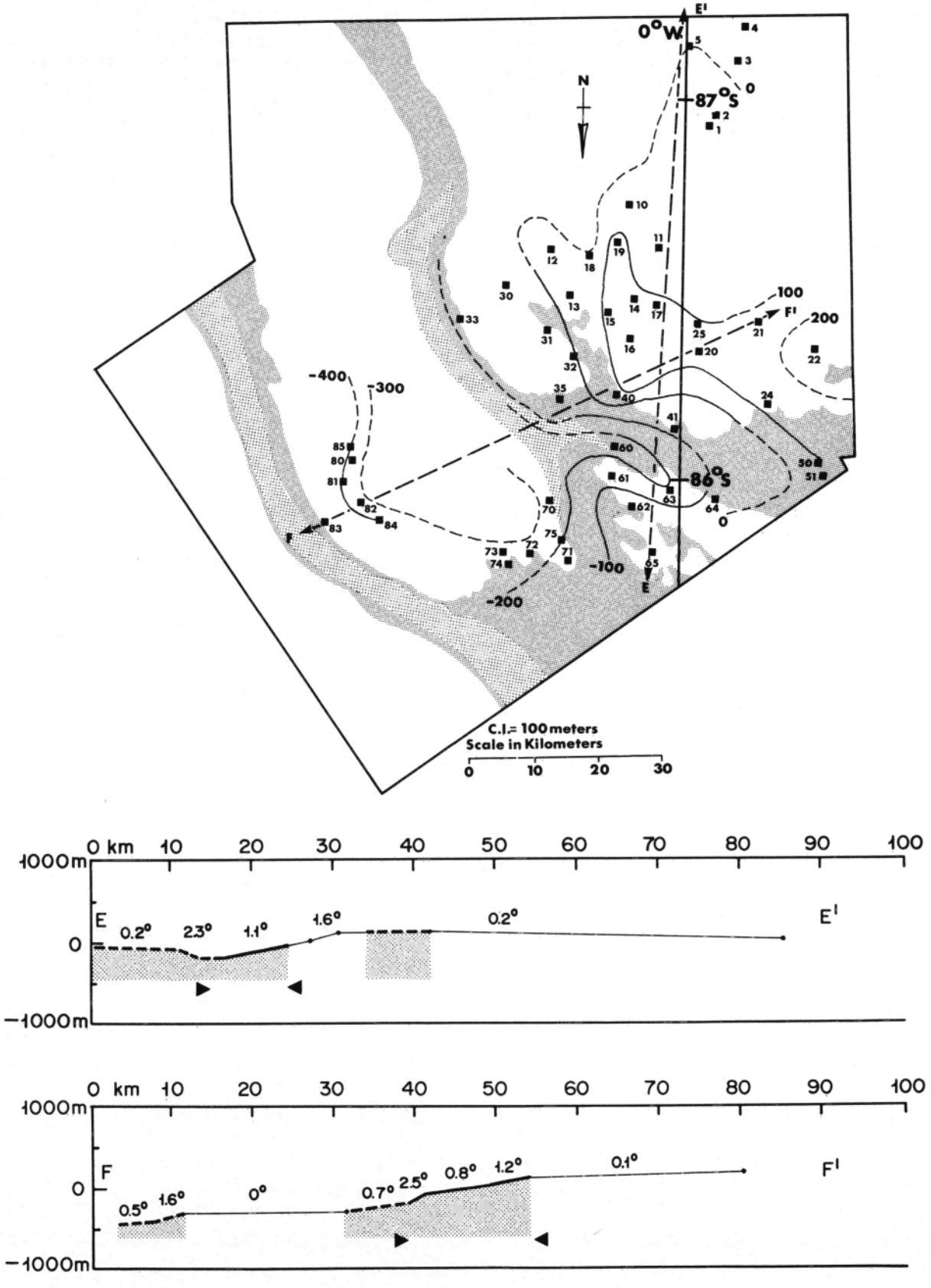

Fig. 5. Model I. Photogrammetric model of an area centered at 86°S, 0°W with associated profiles. Note that the scale of the profiles has been slightly expanded relative to the scale of the photomosaic. Relative elevations for the locations indicated by numbered squares are listed in Table 4; vertical exaggeration in the profiles is 10 : 1. Areas in the profiles bounded by triangles are those in which layers are visible in the best versions of the images; some may not be distinguishable in reproductions. Similarly, stippled areas in the profiles are those which exhibit partial or total defrosting in the best available versions of the photographs. Stippling in the model itself corresponds roughly to relatively low albedo areas in the photomosaic and should be used for visual orientation only.

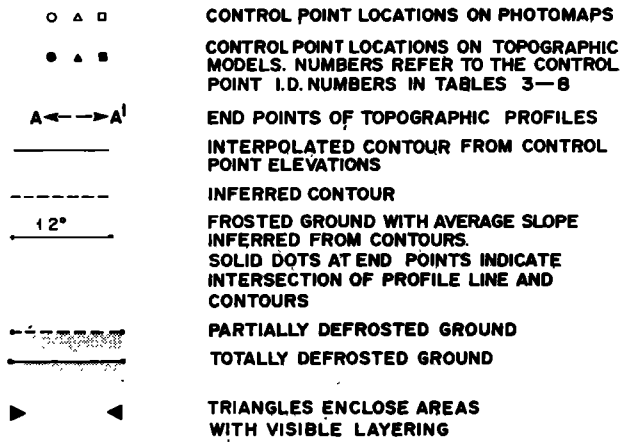

Fig. 6. Key to topographic models.

TABLE 3. Stereo Model A

Control Point	Elevation, m	Control Point	Elevation, m	Control Point	Elevation, m
1	0	15	700	29	1200
2	100	16	300	30	1200
3	0	17	200	31	1500
4	500	18	700	32	1700
5	400	19	800	33	1700
6	1400	20	900	34	2200
7	400	21	1200	35	1600
8	600	22	1600	36	1900
9	700	23	700	37	1200
10	500	24	800	38	1300
11	700	25	1600	39	1500
12	800	26	2200	40	1500
13	1200	27	1900	41	1200
14	700	28	1300	42	1700

Taken together, the occultation, UVS, and A frame photogrammetric data indicate that the south polar layered deposits lie at planetocentric distances ranging from 3378 to 3383 km, with an absolute uncertainty of about 2 km. Similarly, the south polar residual frost cap lies at planetocentric distances ranging from 3381 to 3383 km.

Associated surface pressures above the layered deposits and residual frost can be calculated by assuming that the atmosphere behaves hydrostatically and as an ideal gas. *Kliore et al.* [1973] have shown that the lapse rate of the martian atmosphere near the poles is roughly half of the adiabatic lapse rate. Thus

$$p(z) = p(z_0)\left(\frac{T(z_0) - \Gamma\Delta z}{T(z_0)}\right)^{mg/R\Gamma} \quad (1)$$

where

- $p(z)$ atmospheric pressure at height z;
- $T(z)$ atmospheric temperature at height z;
- z_0 reference height of known pressure, temperature, equal to $z - \Delta z$;
- m atmospheric molecular weight;
- g martian gravitational acceleration, equal to 370 cm/s^2;
- R universal gas constant, equal to 8.31×10^7 ergs/mol/°K;
- Γ atmospheric lapse rate, approximately equal to 2.0°K/km.

In order to minimize errors, pressures have been calculated relative to both the 4.5-mbar equipotential surface computed by *Woiceshyn* [1974] and the 6.1-mbar isobaric surface computed by *Cain et al.* [1973]. Temperatures at both levels were assigned from the occultation data of *Kliore et al.* [1973]. Resulting pressures agree in all cases to within 0.6 mbar.

Surface pressures above the south polar layered deposits are calculated to range from 3.8 to 5.0 mbar, with an uncertainty of about 1.0 mbar. Similarly, pressure above the southern residual frost cap ranges from about 3.8 to 4.3 mbar. The major source of error in these calculations is most likely to be the uncertainty in absolute height associated with errors in the regional tilt of the A frame photogrammetric model. The quoted uncertainty of 1 mbar corresponds to our previous estimate of about 2-km uncertainty in absolute height determinations.

Small-Scale Topography

Five new high-resolution photogrammetric models in the south polar region have now been completed (Figures 4–12; Tables 2, 4–8). Estimated uncertainties in relative elevations of

TABLE 4. Stereo Model I

Control Point	Elevation Relative to Point 32, m	Control Point	Elevation Relative to Point 32, m	Control Point	Elevation Relative to Point 32, m
1	80	21	170	63	−190
2	50	22	240	64	−50
3	−30	24	140	65	−60
4	−130	30	−70	70	−230
5	0	31	−20	71	−130
10	60	32	0	72	−280
11	60	33	−60	73	−280
13	10	35	−70	74	−260
14	100	40	90	75	−200
15	120	41	−100	80	−410
16	160	50	90	81	−380
17	120	51	60	82	−290
18	0	60	−240	83	−440
19	130	61	−120	84	−380
20	120	62	−30	85	−450

TABLE 5. Stereo Model II

Control Point	Elevation Relative to Point 79, m	Control Point	Elevation Relative to Point 79, m	Control Point	Elevation Relative to Point 79, m
1	−375	74	200	114	−460
8	−340	75	0	115	−400
13	−350	77	−85	117	−175
16	−350	78	−50	121	−350
19	−300	79	0	123	0
23	−440	83	−115	124	−360
25	−400	85	−420	125	−330
32	−275	86	−435	128	−430
35	−260	87	−525	131	−460
36	−180	88	−75	135	−220
37	−200	89	−75	140	−125
38	−170	90	−75	147	100
41	−275	91	75	151	40
43	−250	92	−75	154	100
45	−100	93	110	155	160
46	−325	95	135	156	−25
48	−325	96	−360	157	10
52	−285	97	−380	158	−70
54	−240	98	−485	161	−75
57	−260	99	−545	163	−80
58	−215	100	10	166	−180
59	−160	103	60	167	−175
62	−150	104	−220	168	−200
64	−70	105	−120	176	−315
68	75	110	−450	178	−250
69	−20	111	−180	183	−50
71	115	112	−500		
72	110	113	−390		

TABLE 6. Stereo Model III

Control Point	Elevation Relative to Point 34, m	Control Point	Elevation Relative to Point 34, m	Control Point	Elevation Relative to Point 34, m
1	100	34	0	66	−1170
2	−70	35	−170	67	−1150
3	−50	36	−220	68	−1160
4	−410	37	−100	69	−720
5	−520	38	−100	70	−10
6	−730	39	70	71	90
7	−770	40	60	72	−1150
8	−810	42	−370	73	−1270
9	−850	43	−280	74	−1360
10	−190	44	−370	75	−1230
11	210	45	440	80	30
12	240	46	−130	81	450
13	110	47	−140	82	330
14	190	50	−130	83	280
15	−280	51	−510	84	−200
20	650	53	−890	85	−330
21	10	54	−830	86	10
22	−700	55	−680	87	−480
23	−1160	56	−680	88	−120
24	−820	57	−490	90	120
25	−430	58	−690	91	300
26	−400	59	−470	92	480
27	130	60	−330	93	680
28	500	61	−450	94	620
29	1170	62	−970	95	460
30	140	63	−1030	96	740
31	−190	64	−1090	97	800
32	−930	65	−1240	98	940
33	−600				

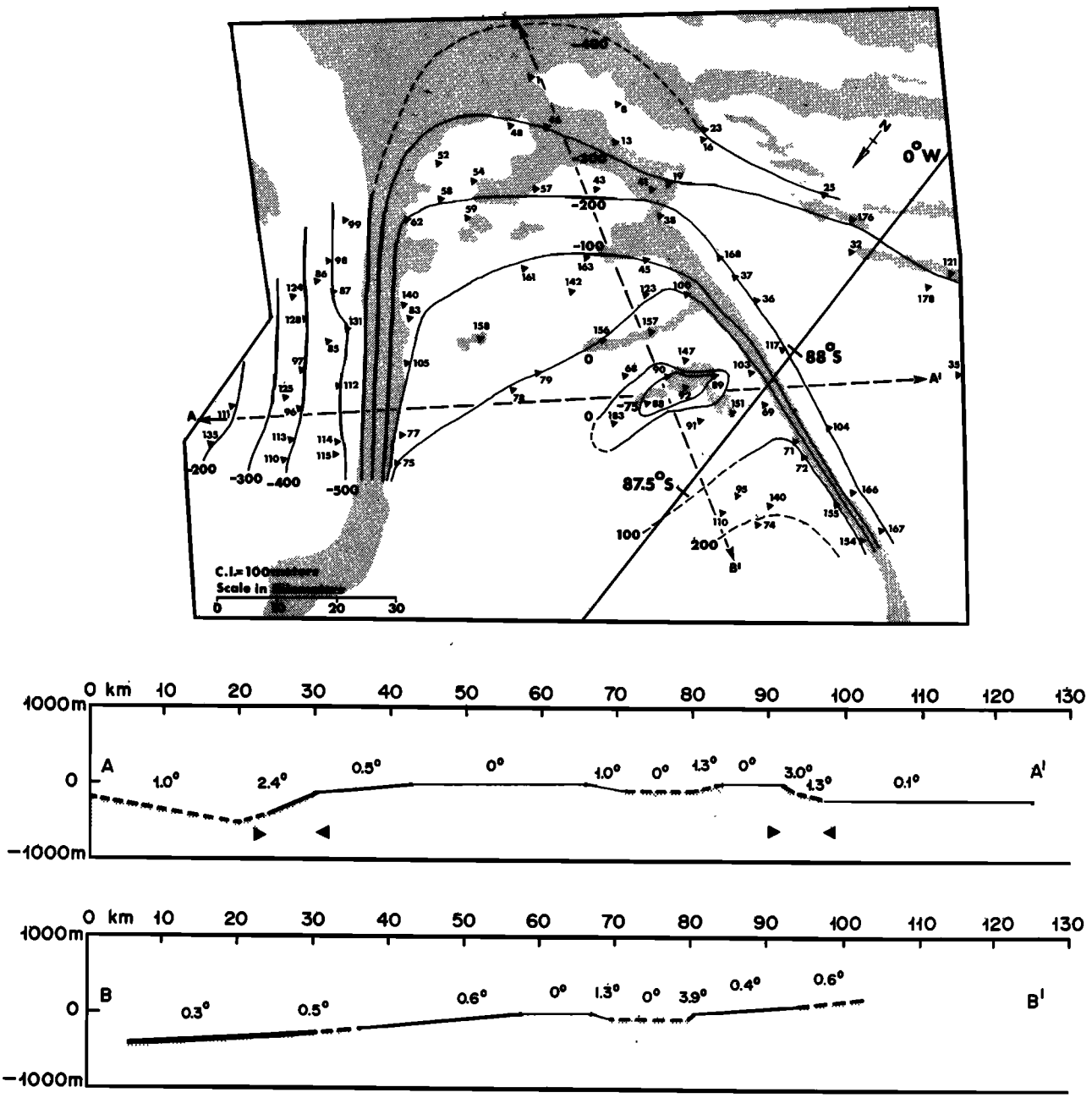

Fig. 7. Model II. Photogrammetric model of an area centered at approximately 88°S, 0°W, which illustrates the morphologies associated with dark bands which are characteristic of both residual polar frost caps. Topographic profiles are drawn with a vertical exaggeration of 10 : 1 and are based on the model's interpolated contours. Numbered triangles indicate locations for which relative elevations have been calculated (Table 5). Note the evidence for topographically controlled defrosting within the dark bands. Horizontal scale of profiles is slightly expanded relative to photomosaic. Contour interval is 100 m.

any two points in a given data network have been calculated from equation (13) of *Blasius* [1973] and are listed for each of the models in Table 2. Also included are ground resolutions for each photograph involved.

The significance of the tilt uncertainty already discussed is apparent in the profiles accompanying models I–V. *Cutts* [1973*a*] has proposed that some of the arcuate dark bands which transect both residual frost caps are erosional troughs associated with complex polar wind patterns, while *Murray and Malin* [1973*a*] have interpreted them as a series of constructional scarps perhaps associated with wandering of the martian spin axis relative to the surface. In an area where the maximum observed slopes are of the order of a few degrees, an uncertainty in the regional tilt of the same magnitude makes the distinction between scarps and troughs a difficult one to draw. (The terms scarp and trough are used here for convenience, even though the observed features are extremely gentle by terrestrial standards.) In several of the profiles, however, no reasonable adjustment of the regional tilt allows one to interpret the discernible topographic features as exclusively troughs or exclusively scarps. Thus the south polar layered deposits exhibit features ranging from scarps to nearly sym-

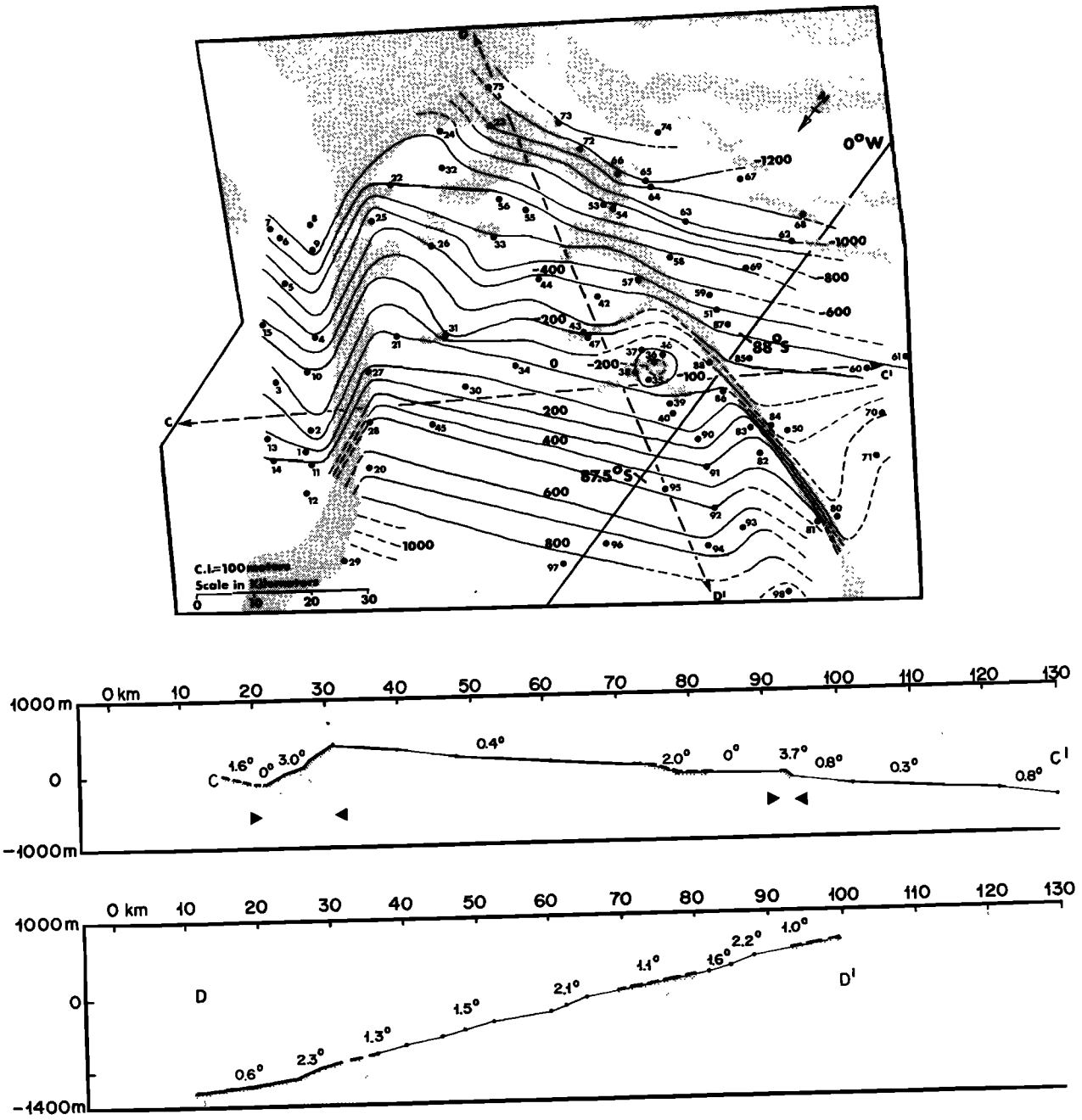

Fig. 8. Model III. Another model of the area included in model II constructed from a different pair of photographs (see Table 2). The two models differ mainly by a regional tilt of about 1.3°, which is within the tilt uncertainty discussed in the text. They agree on the height of features associated with the dark bands to within 100 m. Numbered circles indicate control point locations for which relative elevations have been calculated (see Table 6). Vertical exaggeration in the profiles is 10 : 1; horizontal scale is expanded relative to photomosaic. Contour interval is 100 m.

metric troughs, oriented in such a way that their steepest slope is outward-facing from the central topographic high near 87°S, 0°W.

Models I–V indicate that the south polar bands slope 1°–5° and are 100–1000 m high. Figure 13 emphasizes the extreme subtlety of slopes associated with the bands. From the profiles, roughly 90% of the surface within the cap and sloping 2° or more outward from the central high is partially or totally defrosted. The only two exceptions occur in model III and may result from improper tilt orientation of the entire model. This is consistent with model II of the same area, which differs from model III by a regional tilt of 1.3° and exhibits no such exceptions. In models I–V, only about 30% of the area sloping inward or less than 2° outward from the central high shows evidence of defrosting. Exceptions to these two generalizations, such as partial defrosting of apparently level ground in Models I and II, may result from averaging of local slopes over areas large compared to the dimension of the slopes. Such averaging occurs whenever the data network is not sufficiently dense to resolve individual slopes or where the surface is rough at a scale below the limit of photogrammetric resolution. Note that the above observations do not preclude defrosting of sufficiently steep poleward-facing slopes, as illustrated near 88°–89°S, 0°W (Figure 3).

Fig. 9. Photomosaic of an area centered at approximately 87°S, 90°W, which is included in model IV. Circles enclose point features for which relative elevations have been calculated.

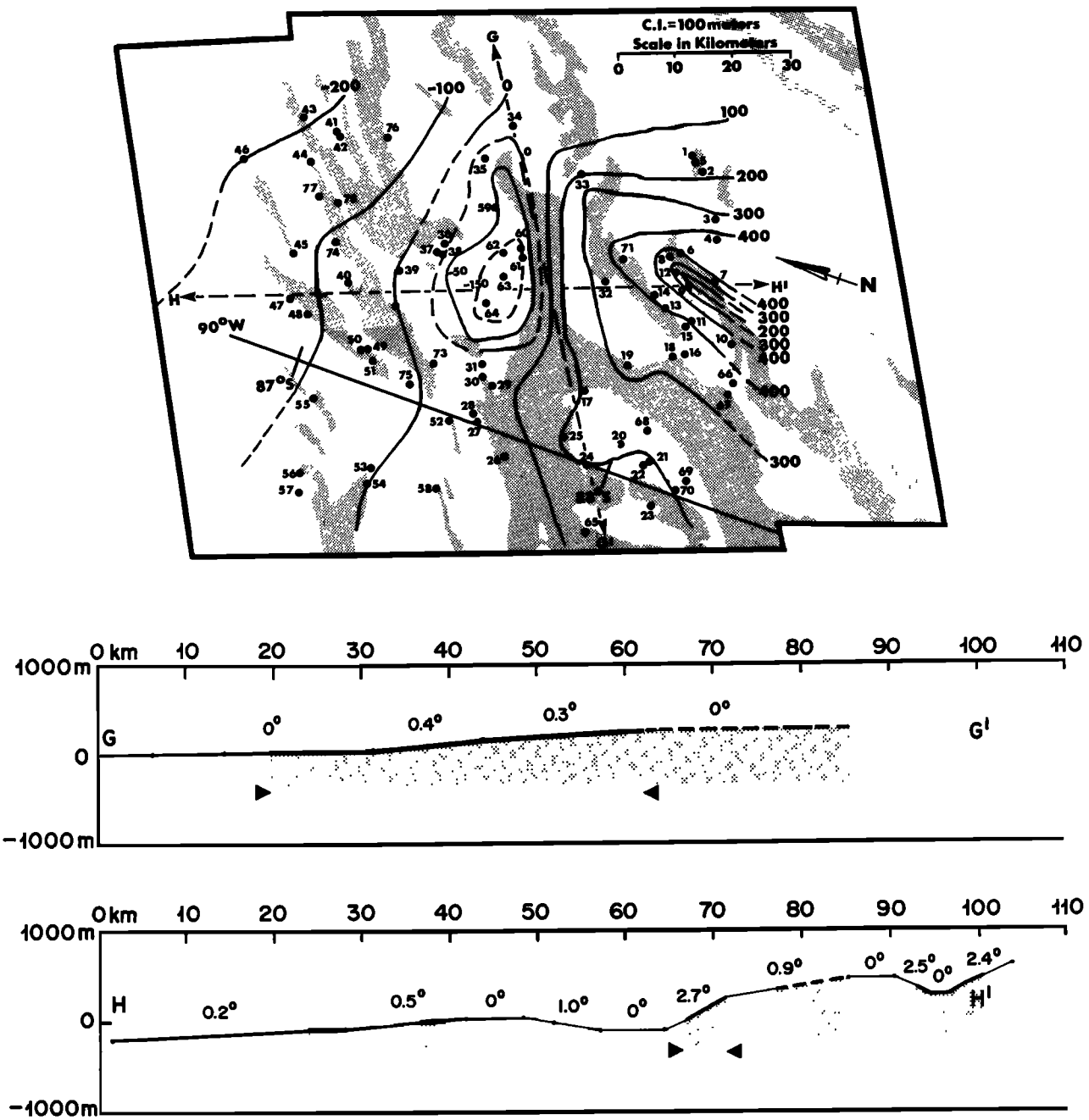

Fig. 10. Model IV. Photogrammetric model showing a variety of topographic forms, including an apparent closed depression near the center. The dark band at about 300-m elevation in the lower right is the same feature as the major scarp shown in Figures 11 and 12. Elevations of the control points indicated by numbered circles are listed in Table 7. Vertical exaggeration in the profiles is 10 : 1; horizontal scale is slightly expanded relative to photomosaic. Contour interval is 100 m.

Taken collectively, the available topographic data suggest that the south polar layered deposits attain a maximum thickness of 1–2 km at a point near 87°S, 0°W. From the UVS data and generalized A frame map (Figure 3), the net relief from the lowest point in the polar basin to the highest point of the layered deposits is approximately 4.5 km. The basin relief in unlayered sections, measured from the floor to the top of the heavily cratered northern rim, is about 3 km (UVS). Thus assuming comparable relief for the buried portion of the basin, 1–2 km of relief can be attributed to the presence of the layered deposits. Under the unlikely assumption that the basin exhibits no relief where buried by the layered deposits, a maximum thickness of 4.5 km could be attributed to the deposits.

North Polar Region

Topographic information concerning the north polar layered deposits is limited to a set of three occultation points (Table 1, Figure 1), an A frame photogrammetric model (model B of Table 2; Table 9; Figures 14, 15), and a single high-resolution B frame model (model VI of Table 2; Table 10; Figures 16, 17). Taken together, the occultation and A frame photogrammetric data imply that the surface of the north polar layered deposits lies at planetocentric distances ranging from 3371 to 3379 km at corresponding atmospheric pressures

TABLE 7. Stereo Model IV

Control Point	Elevation Relative to Point 39, m	Control Point	Elevation Relative to Point 39, m	Control Point	Elevation Relative to Point 39, m
1	180	27	100	53	20
2	160	28	70	54	−30
3	350	29	90	55	−30
4	430	30	130	56	−30
5	210	31	150	57	−80
6	460	32	350	58	30
7	400	33	290	59	−50
8	160	34	80	60	−270
9	190	35	−40	61	−110
10	350	36	−80	62	−200
11	400	37	−80	63	−100
12	280	38	−60	64	−230
13	475	39	0	65	120
14	440	40	−60	66	420
15	400	41	−200	67	375
16	340	42	−170	68	250
17	200	43	−150	69	150
18	340	44	−170	70	230
19	360	45	−130	71	525
20	140	46	190	72	−130
21	260	47	−140	73	30
22	260	48	−110	74	−50
23	170	49	−120	75	−60
24	200	50	−130	76	−160
25	220	51	−130	77	−130
26	75	52	60	78	−175

of 5.0–7.6 mbar (from equation (1)). Similarly, the surface of the northern residual frost cap is calculated to reside at 3373 to 3379 km at pressures ranging from 5.0 to 7.0 mbar.

In the north the A frame model indicates two distinct topographic highs centered near 90°N and 83°N, 0°W. These locations correlate with what appear to be two centers of concentric dark banding visible in Figure 14. In other Mariner 9 photographs taken before final retreat of the north polar seasonal cap (e.g., DAS 12013129) the mottled area covered by the high-resolution B frame model appears morphologically typical of the entire residual cap. The general trend of surface gradients descending from two central highs, combined with details of the B frame model, suggests a series of gentle outward-facing scarps descending stepwise from local topographic highs. The B frame model indicates that these north polar features are 200–1000 m high and exhibit slopes of

TABLE 8. Stereo Model V

Control Point	Elevation Relative to Point 53, m	Control Point	Elevation Relative to Point 53, m	Control Point	Elevation Relative to Point 53, m
1	340	35	285	64	−100
2	360	36	220	67	−100
3	360	37	185	68	−155
4	310	38	200	69	−260
5	250	39	100	71	−100
6	170	40	150	73	−25
8	200	41	125	74	25
9	160	42	100	75	130
10	70	43	60	76	150
11	175	45	115	77	180
12	75	46	50	78	−230
13	175	47	−120	79	−240
14	150	51	−50	80	−180
16	75	52	−25	81	−180
17	125	53	0	82	−200
19	150	54	−50	83	−265
20	25	55	180	85	−715
23	−25	56	180	86	−775
25	−45	57	155	87	−750
26	50	58	−25	88	−1050
28	160	59	−30	89	−1010
29	160	62	−60	90	−800
33	200	63	−40	92	−1000
34	200				

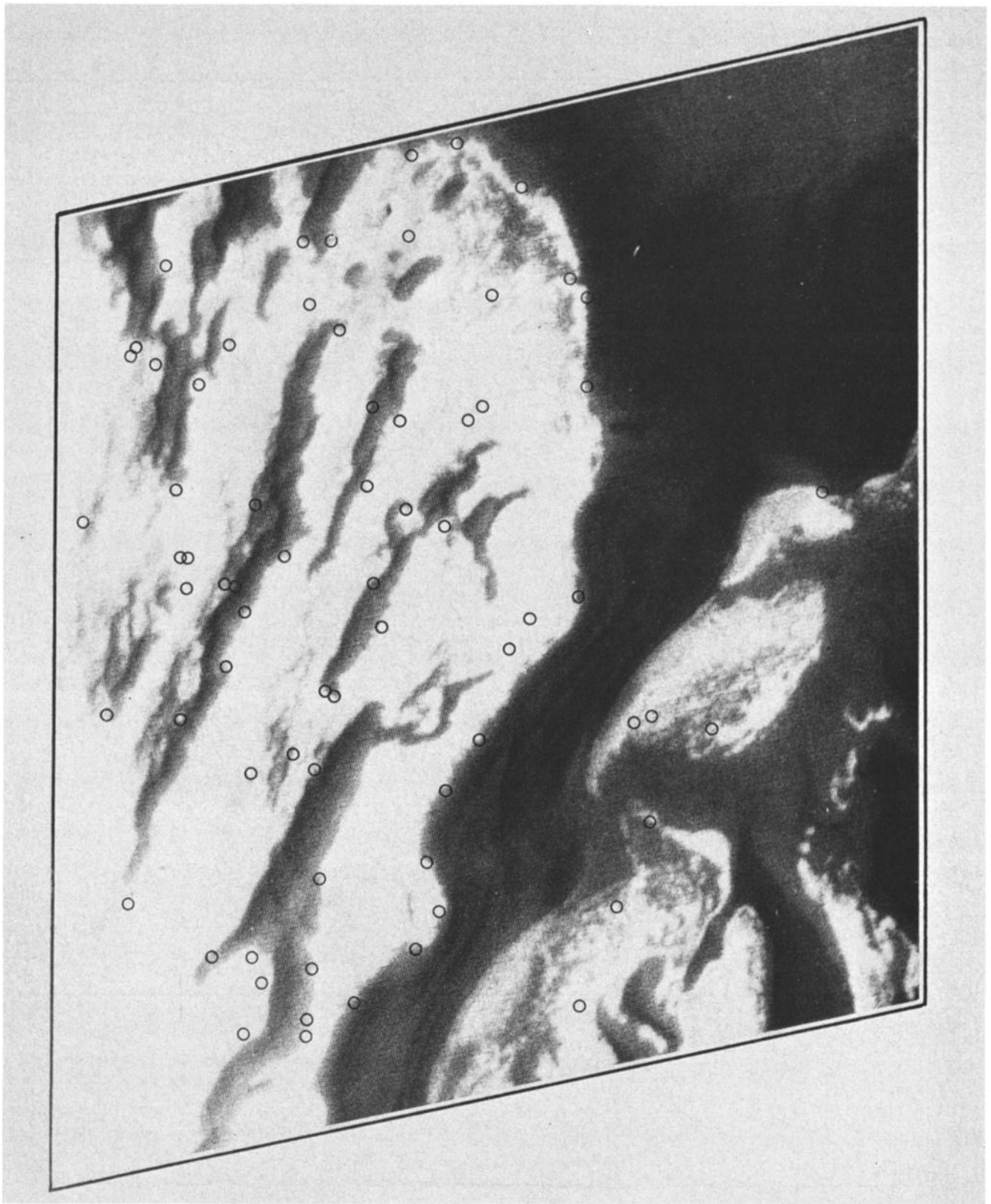

Fig. 11. Photograph of an area centered at approximately 89°S, 90°W, for which high-resolution topography is presented in Figure 12. Note the major layered scarp and several roughly parallel dark features which suggest topographic control of defrosting. Circles enclose point features for which relative elevations have been calculated.

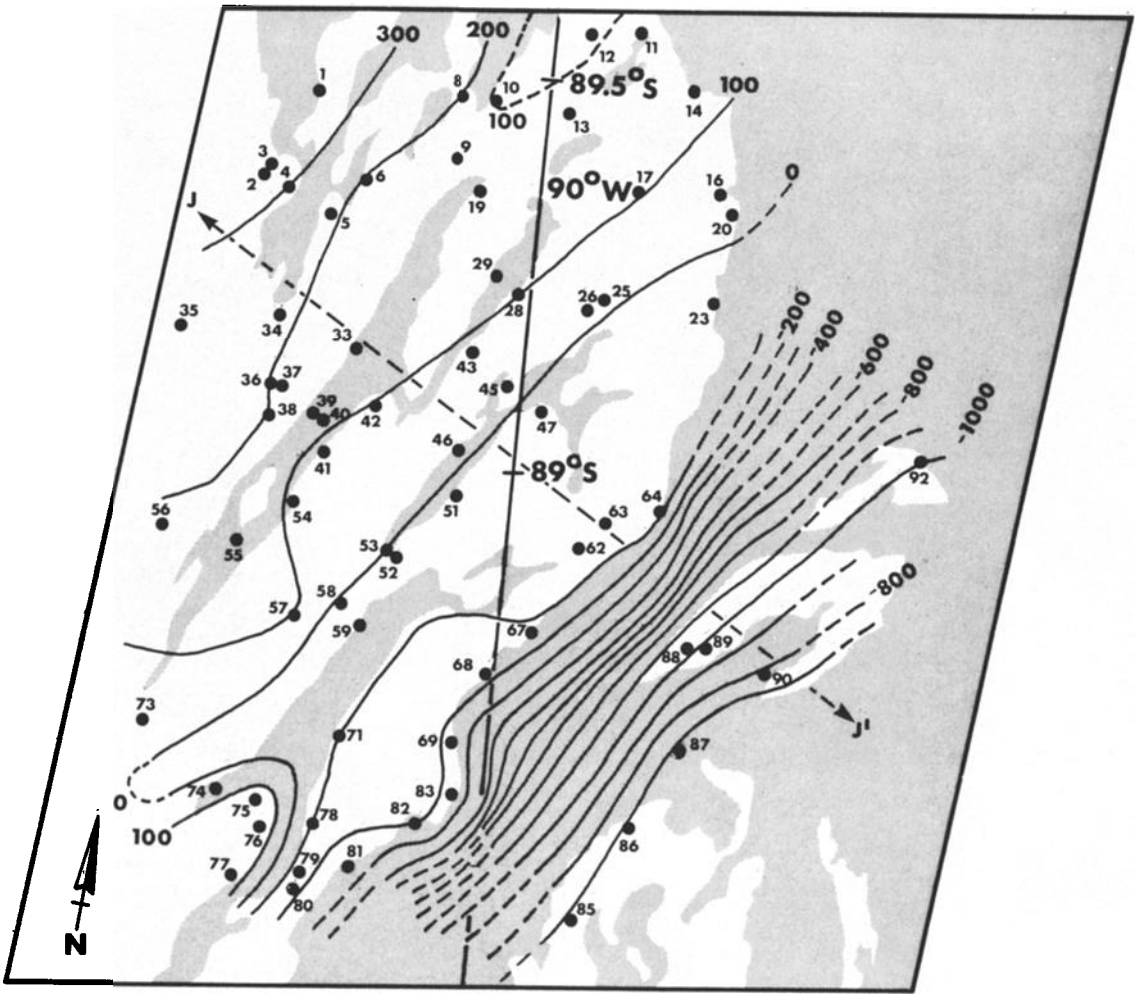

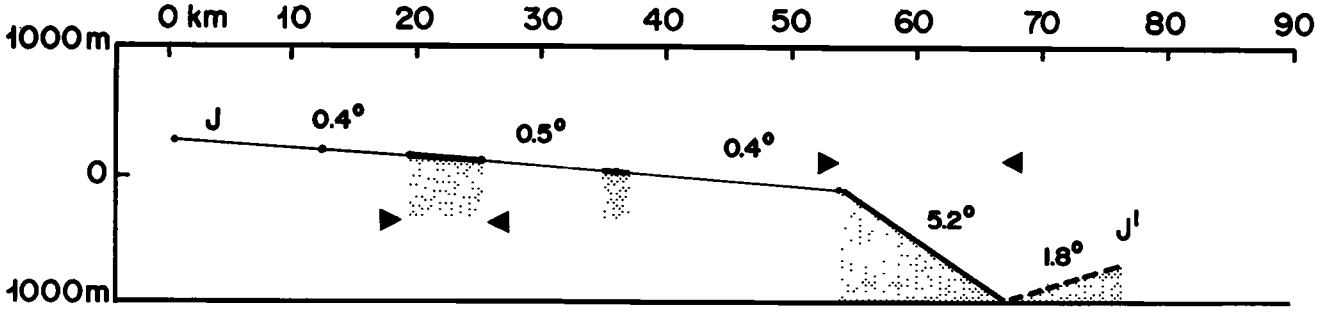

Fig. 12. Model V. Photogrammetric model of a major layered scarp at 89°S, 90°W. Elevations of control points indicated by numbered circles are listed in Table 8. Vertical exaggeration in the profile is 10 : 1; horizontal scale is slightly expanded relative to photograph. Contour interval is 100 m.

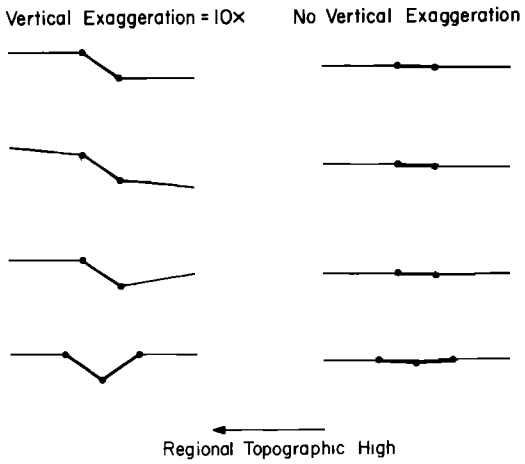

Fig. 13. Generalized topographic features of the south polar layered deposits illustrating the progression from outward-facing scarp to symmetric trough. Note the extreme subtlety of associated heights and slopes. Heavy lines denote defrosted areas.

a few degrees, consistent with similar features seen in the south. In the B frame profile, virtually 100% of the surface within the residual cap and sloping outward 2° or more is partially or totally defrosted. In contrast, only about 35% of the area sloping inward or less than 2° outward is defrosted. By extrapolating a plane under the layered deposits from their perimeter, we estimate the net thickness of the northern deposits to be 4–6 km.

Discussion and Summary

Returning to the framework established at the outset of the paper, we now discuss implications of the topographic data bearing directly on the behavior of polar volatiles and the topographic form of the polar layered deposits.

Implications for the Behavior of Volatiles

High-resolution photogrammetric models of both residual frost caps reveal that in general localized defrosting correlates with a series of outward-facing slopes associated with gentle topographic undulations within the polar layered deposits. Although the topographic data are not sufficiently detailed to permit point-by-point comparisons of intercepted solar flux, observed slopes are in general consistent with the suggestion by *Murray et al.* [1972] that defrosting is controlled by increased solar insolation collected on outward-facing slopes within the layered deposits. However, other processes such as differential erosion of frost along outward-facing slopes or slope-dependent meteorological effects (e.g., 'chinook' winds associated with the eastern Rocky Mountains) could conceivably contribute to the observed defrosting.

This analysis indicates that the south polar layered deposits lie almost entirely at greater elevations than the northern deposits, at variance with a preliminary suggestion by *Soderblom et al.* [1973] that the highest surfaces of each may lie at the same altitude. Height ranges associated with the residual frost caps in both polar regions confirm the conclusion by *Murray and Malin* [1973*b*] that the south polar residual cap lies entirely higher (at lower pressure) than its northern counterpart. *Ward et al.* [1974] have shown that such an elevation difference would cause any hypothetical surface deposit of carbon dioxide in the south to migrate to the north in less than about 2×10^3 years in the absence of some ad hoc mechanism for cooling the south pole relative to the north pole. Since no evidence for such a mechanism exists and since the above time scale is short compared to the short-term obliquity oscillation time scale (1.2×10^5 years), it is doubtful that a perennial CO_2 ice cap would ever form at the south pole. Thus the south pole is an unlikely site for any perennial surface deposit of solid CO_2 and the residual south polar cap is most likely composed of water ice [*Murray and Malin*, 1973*b*; *Ward et al.*, 1974].

Finally, a regional slope of less than 1° in the vicinity of the south pole may serve to shift the point of minimum annual solar insolation away from the pole and thus account for the observed offset of the southern residual cap. Combined with the fact that increased insolation collected on relatively low local slopes is apparently responsible for defrosting the dark bands, this argues that stability of the volatile involved is largely insolation controlled. Location of the cap on a regional topographic high (and consequent pressure low) is evidence that pressure stability is not the critical factor in the offset. This is also consistent with the conclusion that the cap is most likely composed of H_2O and not CO_2 ice.

TABLE 9. Stereo Model B

Control Point	Elevation, km	Control Point	Elevation, km	Control Point	Elevation, km	Control Point	Elevation, km
1	−9.8	21	−4.8	41	−3.2	61	−1.0
2	−9.3	22	−4.4	42	−5.2	62	3.4
3	−6.0	23	−4.1	43	−9.6	63	2.9
4	−5.8	24	−4.6	44	−7.4	64	3.2
5	−6.7	25	−3.0	45	−7.5	65	3.2
6	−4.0	26	−3.7	46	3.1	66	−0.6
7	−3.5	27	−2.8	47	0.8	67	1.0
8	−4.4	28	0.4	48	1.0	68	0.2
9	−12.0	29	0.9	49	−5.9	69	1.2
10	−6.3	30	3.4	50	−6.2	70	1.2
11	−10.0	31	0.2	51	1.6	71	1.5
12	−9.5	32	−1.5	52	−5.3	72	1.7
13	−12.3	33	−1.0	53	−5.7	73	1.8
14	−11.7	34	−0.4	54	−2.5	74	2.1
15	−11.2	35	0.1	55	−2.4	75	0.5
16	−6.0	36	−1.7	56	−0.4	76	−1.0
17	−1.9	37	−0.3	57	−6.2	77	1.0
18	−2.5	38	−0.2	58	−5.4	78	0.7
19	−2.9	39	−0.3	59	−2.3	79	3.0
20	−4.3	40	−2.8	60	−2.6	80	2.5

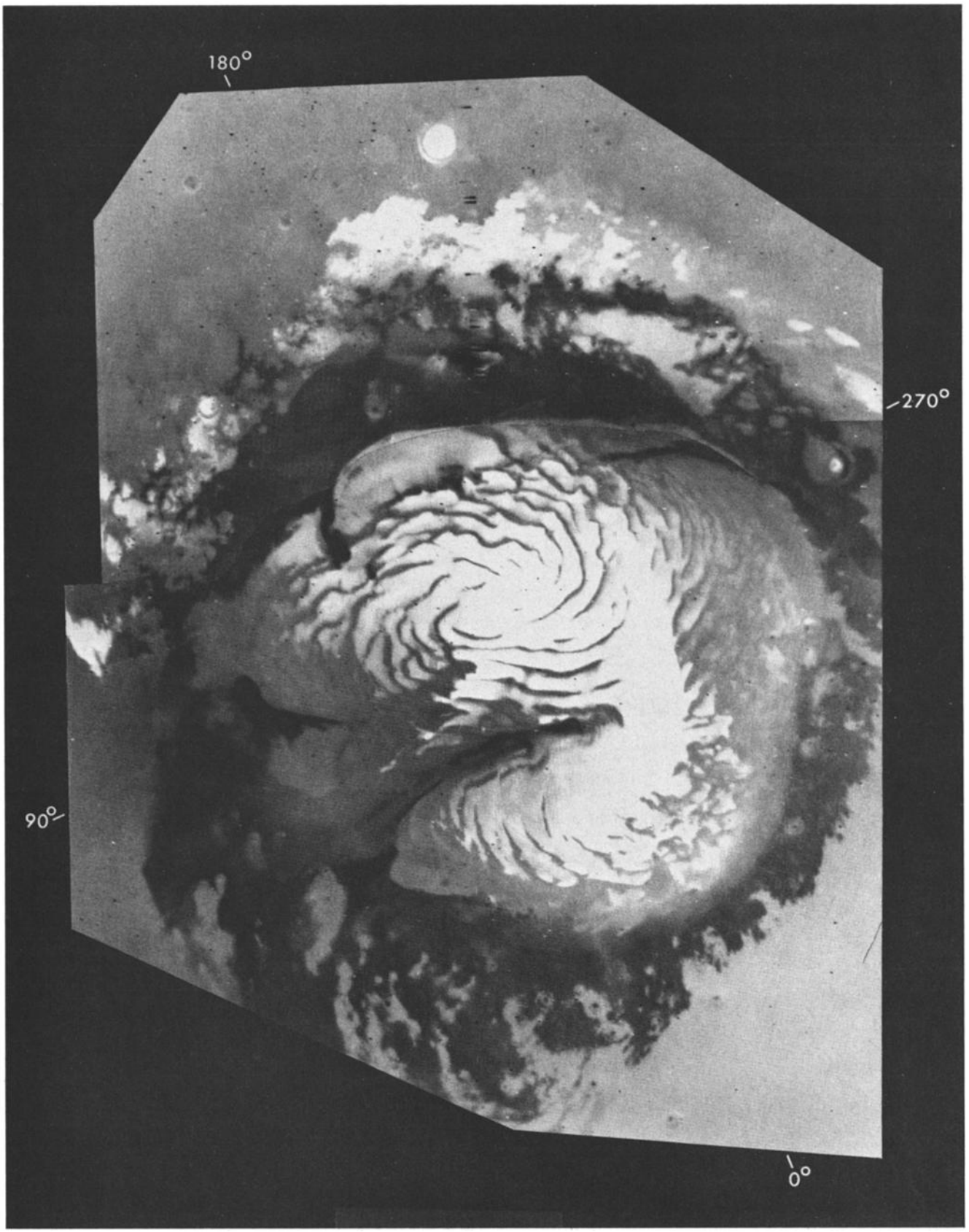

Fig. 14. Photomap of the north polar residual frost cap at A frame resolution illustrating its banded appearance and distinctive bimodal form. Topographic information indicates that the bands arise from defrosting of a series of outward-facing scarps descending steplike from two central topographic highs centered at 90°N and 83°N, 0°W, respectively. Two photographs which comprise the mosaic have been computer enhanced at the Image Processing Lab of NASA's Jet Propulsion Laboratory.

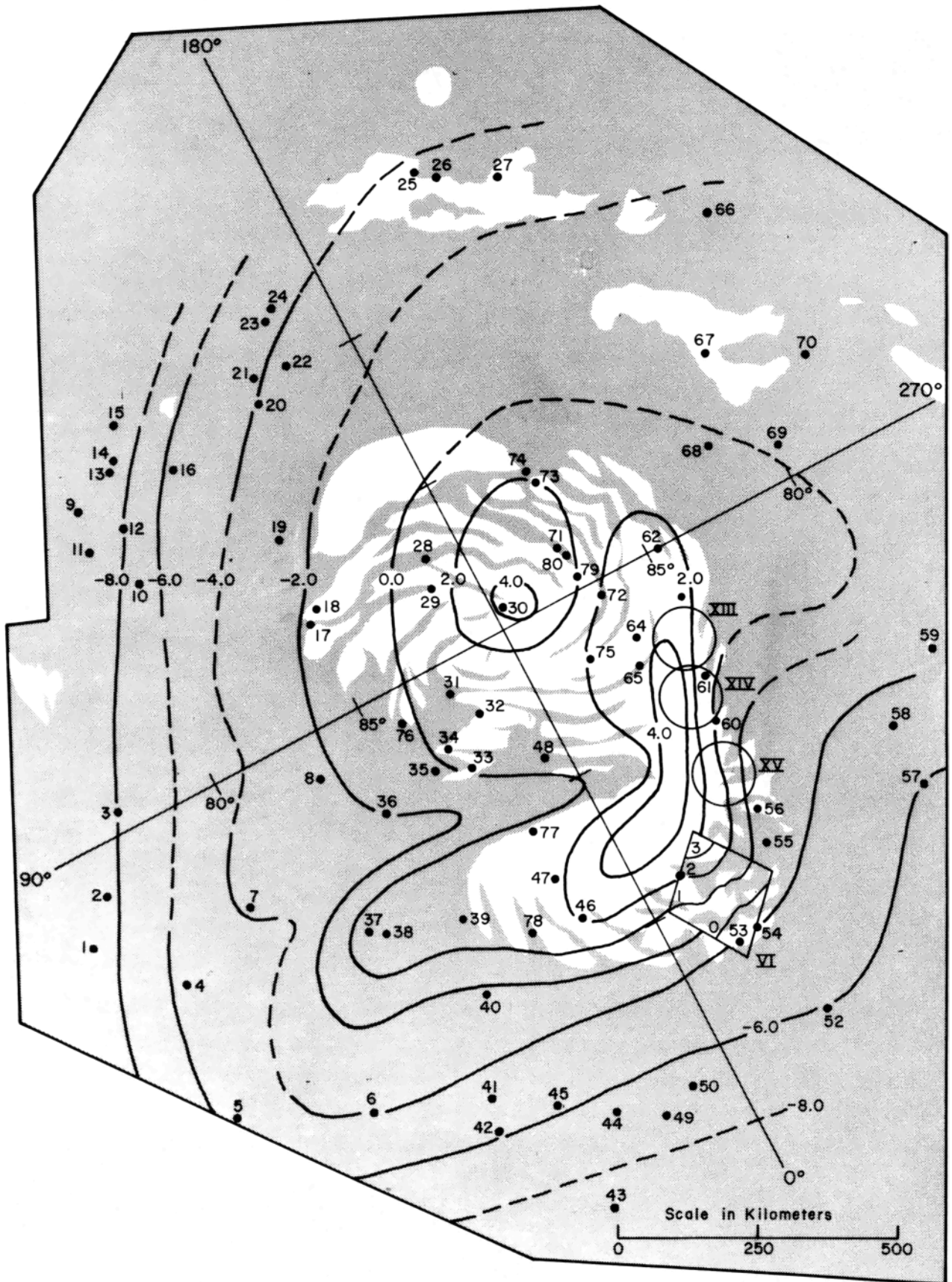

Fig. 15. Generalized topographic map of the north polar residual frost cap produced by combining a wide-angle A frame model (model B) with a single high-resolution B frame model (model VI). Included are the locations of three radio occultation points for which absolute radii and associated surface pressures are listed in Table 1. The original model has been tilted about 0.3° around the axis defined by the occultation points, so that the boundaries of the layered deposits at the top and bottom of the model now lie at the same height. Point elevations for model B are listed in Table 9. Planetary curvature associated with a spherical planet with a radius of 3379 km has been removed from both models. Contour interval is 2 km.

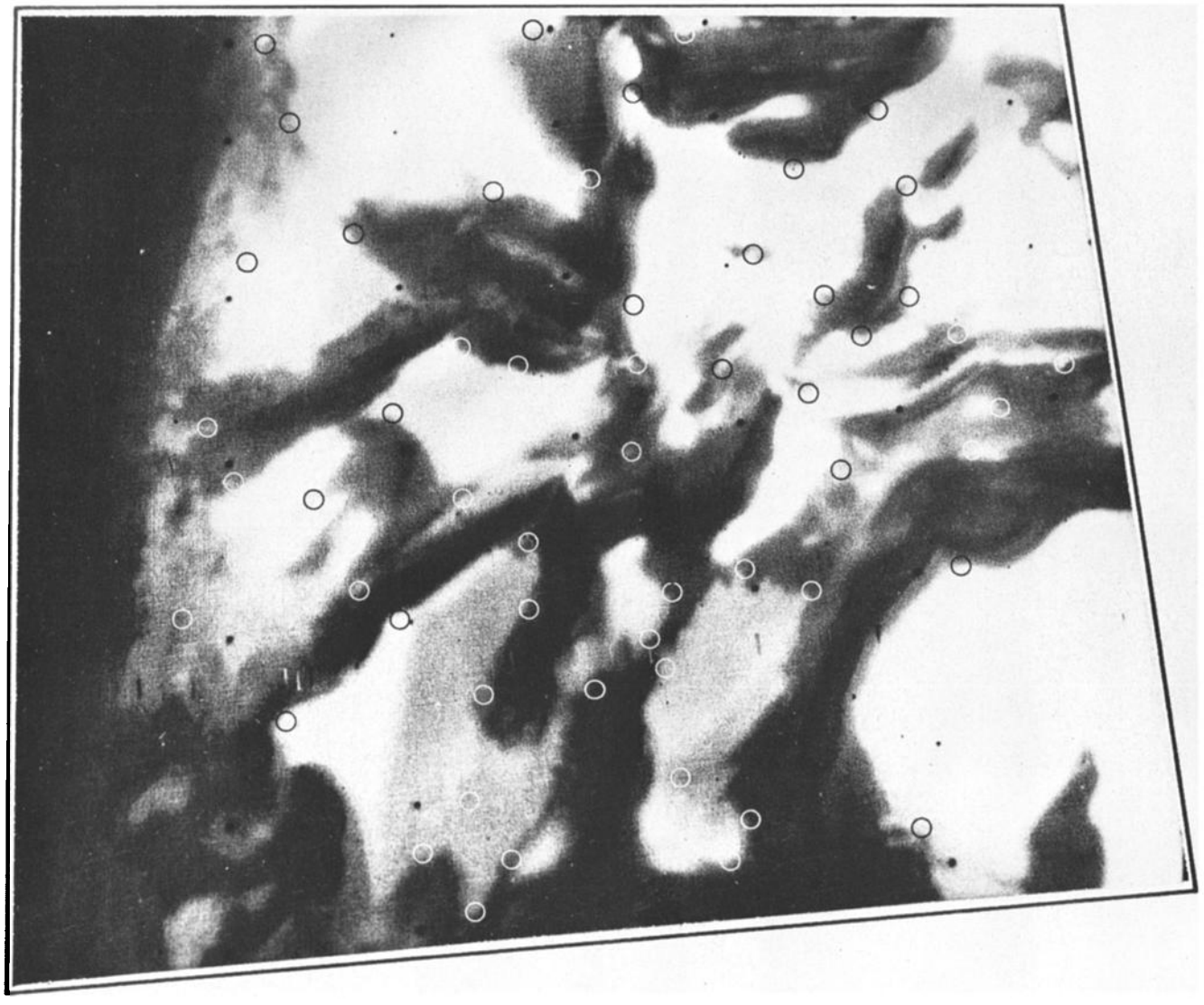

Fig. 16. Photograph of one area in the north polar region for which high-resolution topography was obtained. Circles enclose features for which relative elevations have been calculated.

TABLE 10. Stereo Model VI

Control Point	Elevation Relative to Point 5, m	Control Point	Elevation Relative to Point 5, m	Control Point	Elevation Relative to Point 5, m
1	−300	20	2550	39	1150
2	600	21	2150	40	1800
3	250	22	2100	41	1550
4	1050	23	2000	42	1400
5	0	24	1950	43	1550
6	−100	25	800	44	2350
7	150	26	1000	45	2150
8	650	27	1100	46	1750
9	800	28	1100	47	2150
10	1650	29	700	48	2000
11	1950	31	850	49	3050
12	1050	32	1050	50	3450
13	1300	33	550	51	2150
14	1100	34	300	52	1850
15	2100	35	650	53	2350
16	2350	36	400	54	2100
17	2100	37	900	55	2350
18	2500	38	950	56	1650
19	2550			57	1700

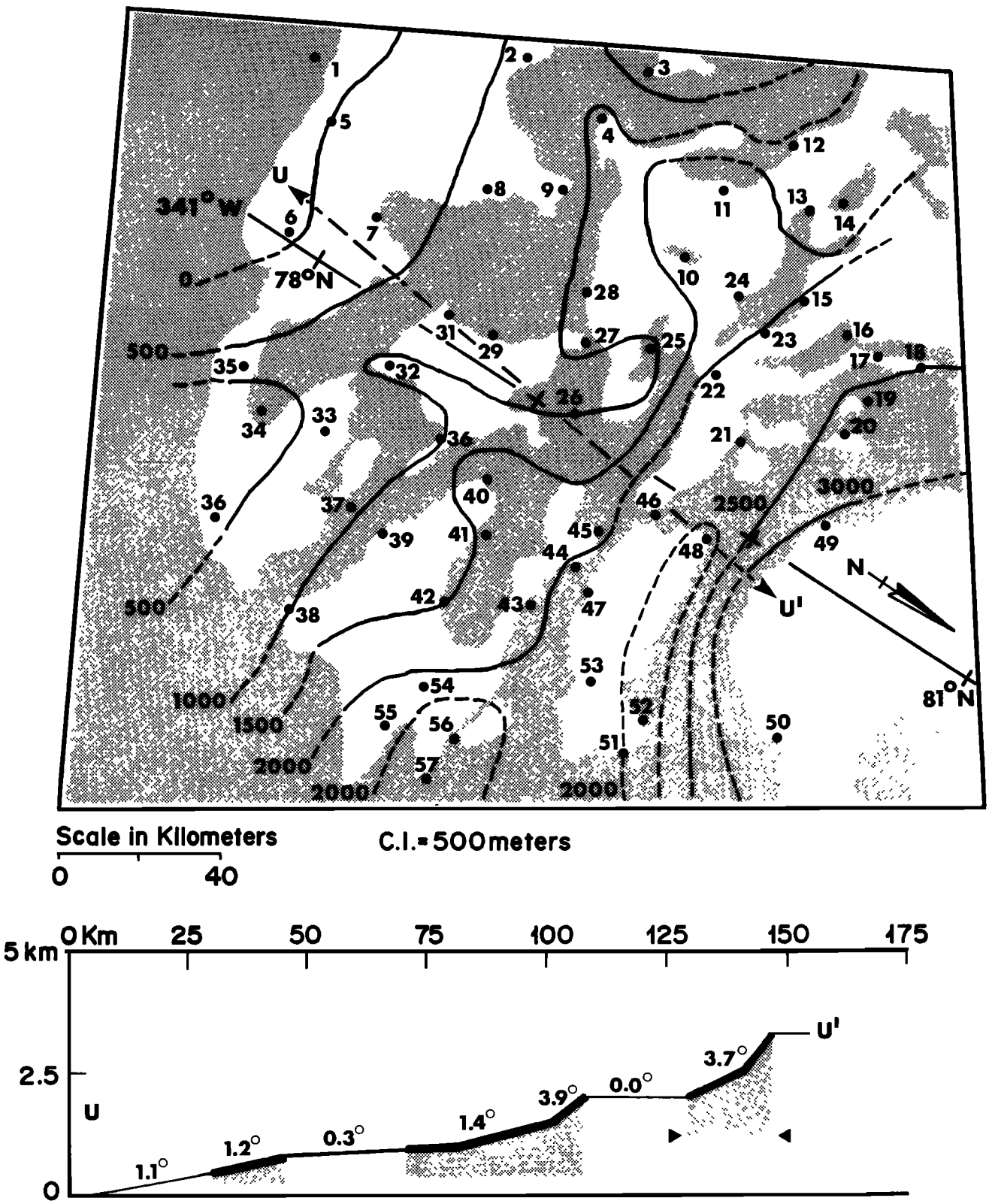

Fig. 17. Model VI. Photogrammetric model of the north polar area centered at approximately 79°N, 345°W. Note the apparent steplike morphology and topographic control of defrosting indicated by the profile. Note also the large amount of relief across the dark areas compared to similar features in the south. Elevations of control points indicated by numbered circles are listed in Table 10. Vertical exaggeration in the profile is 10 : 1; horizontal scale is slightly expanded relative to photograph. Contour interval is 500 m.

Topographic Configuration of the Polar Layered Deposits

Consistent with the data already presented, we offer the following semiquantitative topographic description of the polar layered deposits. In both the north and the south a series of regularly spaced outward-facing topographic undulations sloping from 1°–5° and ranging in height from 100 to 1000 m descend from central topographic highs. In the south a single high is centered near 87°S, 0°W, while the north displays a pair of distinct highs centered near 90°N and 83°N, 0°W, respectively. Topographic features within the south polar layered deposits exhibit the full range of morphologies from trough to scarp, while observed features of the northern deposits appear to be more exclusively scarplike. However, the apparent difference could result from limited stereo coverage of the northern deposits.

Cutts [1973*a*] has pointed to the westward curvature of large erosional reentrants within the south polar basin and between the lobes of the north polar residual cap as evidence for the action of Coriolis-affected polar winds. Dark bands in the north polar residual cap exhibit exclusively eastward curvature, while similar features in the southern cap exhibit both eastward and westward curvature (Figures 2 and 14). It seems unlikely therefore that topographic features represented by the bands can generally be ascribed to aeolian erosion by Coriolis-affected winds. The suggestion by *Cutts* [1973*a*] that a more complex wind pattern near the poles may be responsible for erosion of the dark bands remains a viable but purely speculative alternative.

Layered deposits in each polar region lie at significantly different planetocentric distances, the southern deposits lying almost entirely above their northern counterparts. Total thickness of the polar deposits is 1–2 km in the south and 4–6 km in the north.

The topographic configuration of the polar deposits which emerges from the Mariner 9 data is more complex than would be expected from either the purely constructional model of *Murray and Malin* [1973*a*] or from the purely erosional model of *Cutts* [1973*a*]. More realistic genesis models for the deposits probably require both constructional and erosional processes to account for their observed topographic complexity. Future acquisition of high-quality polar topographic data would contribute to our better understanding of the behavior of polar volatiles and the genesis of the polar layered deposits and thus should be a prime goal of future spacecraft missions to Mars.

Acknowledgments. We wish to acknowledge the contributions made by Bruce C. Murray and Michael C. Malin during many hours of animated discussion. We also thank Clark R. Chapman, James A. Cutts, Charles W. Hord, Andrew P. Ingersoll, Carl Sagan, and Robert P. Sharp for their careful reviews of the manuscript. The generosity displayed by Hord and Pang in consenting to our presentation of their preliminary results is especially noteworthy. Special thanks are also due to Jurrie J. van der Woude for his patience and skill in the preparation of illustrations and to the personnel of the Image Processing Lab of NASA's Jet Propulsion Laboratory for their expert assistance in the computer enhancement of images used in the paper. This work represents one phase of research being conducted at the Space Photography Laboratory of the California Institute of Technology under NASA grant NGR 05-002-305. Contribution 2410, Division of Geological and Planetary Sciences, California Institute of Technology, Pasadena, California.

REFERENCES

Blasius, K. R., A study of martian topography by analytic photogrammetry, *J. Geophys. Res., 78,* 4411, 1973.

Cain, D. L., A. J. Kliore, B. L. Seidel, M. J. Sykes, and P. Woiceshyn, Approximations to the mean surface of Mars and Mars atmosphere using Mariner 9 occultations, *J. Geophys. Res., 78,* 4352, 1973.

Conrath, B., R. Curran, R. Hanel, V. Kunde, W. Maguire, J. Pearl, J. Pirraglia, J. Welker, and T. Burke, Atmospheric and surface properties of Mars obtained by infrared spectroscopy on Mariner 9, *J. Geophys. Res., 78,* 4267, 1973.

Cutts, J. A., Wind erosion in the martian polar regions, *J. Geophys. Res., 78,* 4211, 1973*a*.

Cutts, J. A., Nature and origin of layered deposits of the martian polar regions, *J. Geophys. Res., 78,* 4231, 1973*b*.

Hord, C. W., C. A. Barth, A. I. Stewart, and A. L. Lane, Mariner 9 ultraviolet spectrometer experiment: Photometry and topography of Mars, *Icarus, 17,* 443, 1972.

Hord, C. W., K. E. Simmons, and L. K. McLaughlin, Mariner 9 ultraviolet spectrometer experiment: Pressure-altitude measurements on Mars, *Icarus, 21,* 292, 1974.

Kliore, A. J., G. Fjeldbo, B. L. Seidel, M. J. Sykes, and P. M. Woiceshyn, *S* band radio occultation measurements of the atmosphere and topography of Mars with Mariner 9: Extended mission coverage of polar and intermediate latitudes, *J. Geophys. Res., 78,* 4331, 1973.

Murray, B. C., and M. C. Malin, Polar wandering on Mars?, *Science, 179,* 997, 1973*a*.

Murray, B. C., and M. C. Malin, Polar volatiles on Mars–Theory vs. observations, *Science, 182,* 437, 1973*b*.

Murray, B. C., L. A. Soderblom, J. A. Cutts, R. P. Sharp, D. J Milton, and R. B. Leighton, Geological framework of the south polar region of Mars, *Icarus, 17,* 328, 1972.

Pang, K., Ultraviolet reflectance of Mars' south polar cap and opacity of the 1971 dust cloud, Annual Meeting of American Astronomical Society Division for Planetary Science, University of Hawaii, Honolulu, Hawaii, March 21–24, 1972.

Soderblom, L. A., M. C. Malin, J. A. Cutts, and B. C. Murray, Mariner 9 observations of the surface of Mars in the north polar region, *J. Geophys. Res., 78,* 4197, 1973.

Ward, W. R., B. C. Murray, and M. C. Malin, Climatic variations on Mars, 2, Evolution of carbon dioxide atmosphere and polar caps, *J. Geophys. Res., 79,* 3387, 1974.

Wilhelms, D. E., Comparison of martian and lunar multiringed circular basins, *J. Geophys. Res., 78,* 4084, 1973.

Woiceshyn, P. M., Global seasonal atmospheric fluctuations on Mars, *Icarus, 22*(3), 325, 1974.

(Received December 12, 1974;
revised March 24, 1975;
accepted March 31, 1975.)